Swansea University
Prifysgol Abertawe

Cronfa
Setting Research Free

Cronfa - Swansea University Open Access Repository

_____

This is an author produced version of a paper published in :
Sensors and Actuators A: Physical

Cronfa URL for this paper:
http://cronfa.swan.ac.uk/Record/cronfa22713

_____

Paper:

Mei, J. & Li, L. (2015). Double-wall piezoelectric cylindrical energy harvester. *Sensors and Actuators A: Physical, 233*
, 405-413.

http://dx.doi.org/10.1016/j.sna.2015.07.022

_____

Accepted Manuscript

Title: Double-wall piezoelectric cylindrical energy harvester

Author: Jie Mei Lijie Li
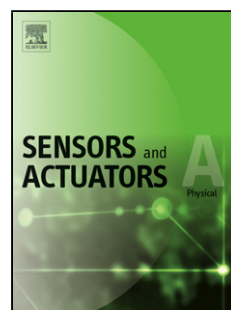
Please cite this article as: J. Mei, L. Li, Double-wall piezoelectric cylindrical energy harvester, *Sensors and Actuators: A Physical* (2015), http://dx.doi.org/10.1016/j.sna.2015.07.022

Double-wall piezoelectric cylindrical energy harvester

Jie Mei and Lijie Li

College of Engineering, Swansea University, Swansea, SA2 8PP, UK
Corresponding email: L.Li@swansea.ac.uk

Abstract: Cylindrical structures possess the advantage of responding multi-directional vibrations compared with cantilevers. In this paper a double-wall cylindrical energy harvesting device is proposed to scavenge multi-mode mechanical vibrations. Compared with the single wall energy harvester, it is found from the finite element analysis that the double wall device generates higher output voltage, and responds to a wider oscillating frequency range. These advantages have been validated by experiments, where the open circuit output voltage for eight resonating modes has been characterized. For further investigation, dynamic responses of the device at these eight resonating modes have been characterized under various excitations. It is seen from the experiment that as the driven voltage of the excitation source increases from 5 V to 16 V, the output voltage increases and the corresponding quality factors reduces.

Keywords: Double-wall cylindrical structure, energy harvesting, piezoelectric

1

1. Introduction

During the past decades, energy harvesters have been widely used in wireless sensor networks [1], mechanical structure health monitoring systems [2] and micro-air-vehicles powering units [3]. Energy harvesting can be achieved by transferring solar [4], thermal and mechanical energy [5] into electricity. Since the mechanical vibration is commonly available, the vibrational energy harvesting devices have been intensively researched. Vibrational energy harvesters are normally categorized into three types in terms of transduction mechanism, which are electromagnetic [6], electrostatic [7] and the piezoelectric [8]. This paper focuses on the piezoelectric vibrational energy harvesting devices. Several mechanical structures and operating mechanisms have been reported for piezoelectric vibrational energy harvesters. The rectangular cantilever is a general form of the energy harvesting device as it is easy to realize [9]. With the same volume of rectangular beam, Roundy et al. [10] devised a triangular trapezoidal beam achieving a better output performance. However, the cantilever devices are only effective in the first bending mode. In order to harvest multiple oscillating frequencies, Liu et al. [11] have fabricated an array of piezoelectric cantilevers with different lengths to respond more resonating frequencies. Schaufuss et al. [12] reported an approach by adjusting the position of the auxiliary mass to tune the external vibrating frequency. Liu et al. [13] proposed a double-mode energy harvester by placing an oscillator at the tip of the cantilever beam. Zhou et al. [14] achieved a novel energy harvester that enables harvesting energy from multimode resonance by introducing the multimode intermediate beam. Although the above developments have successfully improved the working efficiency, their configurations were complex and should be operated with the help of the auxiliary systems. In addition to the cantilever beam, Lee and Youn [15, 16] introduced the concept of the multimodal energy harvesting skin to harvest the mechanical energy from multimode vibrations. Spiral-shape cantilever beam have been designed to harvest multiple resonant frequencies [17] [18]. The piezoelectric cylindrical shell can be a potential structure to harvest multi-modal vibrations in real applications as it can be easily

2

excited into both transverse and thickness shear vibrations [19, 20]. Piezoelectric cylindrical shell has been widely used in ultrasonic motors [21], sensors [22] and resonators [23]. Models of tri-axial sensors and actuators made of a single piezoelectric cylindrical shell have been reported by Wakatsuki et al. [24] Mazeika et al. proposed a new cylindrical piezoelectric actuator in which electrodes were segmented into several patches for verifying multimode responses [25]. Li and Tzou demonstrated a piezoelectric cylindrical vibrating energy harvester model to show the basic multi modal energy distribution in numerical methods [26]. This mechanism was later verified by their experimental study in a piezoelectric ring energy harvester in 2013 [27]. However, their models are all in simple support boundary conditions, which is different with our proposed clamped-free prototype. Furthermore, double cylindrical shells are reported in this paper for improving output electrical power and widening operation frequencies. The mechanical dynamic and vibration behaviors have been investigated in [28] [29] [30], it is a new approach to use it in energy harvesting applications. The rest of this paper is structured as follows: Schematic design of the double wall cylindrical structure is shown in section 2. Numerical analysis is conducted in section 3. It follows by the description of experiment in section 4. Finally, conclusions are drawn in section 5.

2 Schematic design of the device

Schematic configuration of the double-wall piezoelectric cylindrical energy harvester is shown as Figure 1(a). This device mainly consists of two steel cylindrical shells and a fixture. The fixture was machined into an L-shape so that the inertial masses move perpendicularly to the longitudinal axis of the cylinder to induce transverse motions. In order to enhance the fixture stiffness, two triangular ribbed plates were also welded along the L-shape plate edges. One end of the inner cylinder (Figure 1(c)) was welded to the fixture directly, and the other end was attached with a proof mass. To make sure the outer cylinder gets through the inner

3

shell, the proof mass was placed inside of the inner cylinder. Similarly, one end of the outer cylinder (Figure 1(d)) was welded through a square connecting plate with screw holes and the other end was attached with a proof mass. The outer cylindrical shell was assembled co-axially with the inner wall. The whole assembled structure is excited with a vibrating source. Figure 1(b) shows the cross-section of the double-wall cylindrical device. The symbols $R_i, R_o, \alpha, t_i, t_p$ and t_o represents the inner wall radius, outer wall radius, curved angle of piezoelectric layer, inner wall thickness, piezoelectric layer thickness and outer wall thickness. The values for them are 3mm, 5mm, 75.4°, 0.8mm, 0.11mm and 0.8mm respectively. Figures 1(c) and 1(d) show the detailed structures of both the inner and outer cylindrical shells. Lengths of the inner cylindrical shell, piezoelectric layer and outer cylindrical shell are 101mm, 50mm and 100mm. The radius and length of the inner proof mass are 3mm and 15mm. The inner radius, outer radius and length of outer proof mass are 5.8mm, 20.8mm and 15mm. The piezoelectric layer is placed 10mm away from the fixed end to leave enough space for the electric wire. Based on the direct piezoelectric effect, the vibration of the structure will induce charges on the surface of the piezoelectric layer. Simulation of the structure is conducted in the following section.

3 FEM simulations of cylindrical energy harvesting device

FEM (finite element method) simulations of the proposed cylindrical device are conducted using the software package ANSYS 12.0. In the numerical simulation, the piezoelectric layer is modeled by element Solid226. The external load resistor is included in the simulation using element type Circu94. Solid186 is used to model remaining mechanical structures. Dimensions of the model are set according to the design dimensions of the device. As for the material properties, we choose the PVDF for the piezoelectric material and mild steel for cylindrical substrate and remaining mechanical structures. The density, Poisson ratio and

4

Young's modulus of mild steel are 7860kg/m^3, 0.3 and 210 GPa respectively. As the curved piezoelectric layer is polarized in the radius direction, and cylindrical coordinate system in ANSYS is set as (r, θ, z) in default, the stiffness matrix c_{ANSYS}^E, the piezoelectric coupling matrix e_{ANSYS} and the dielectric coefficient matrix ε_{ANSYS} are detailed in equation (1). Values for the elasticity stiffness, the piezoelectric stress coefficients and the dielectric coefficients of PVDF material are designated as $c_{11} = c_{22} = c_{33} = 3.933 Gpa$, $c_{12} = c_{21} = c_{13} = c_{31} = c_{23} = c_{32} = 1.6075 Gpa$, $c_{44} = c_{55} = c_{66} = 1.1628 Gpa$, $e_{13} = e_{23} = 0.0744 C/m^2$, $e_{33} = -0.0558 C/m^2$, $\varepsilon_{11} = \varepsilon_{22} = \varepsilon_{33} = 12$.

$$c_{ANSYS}^E = \begin{bmatrix} c_{33} & c_{32} & c_{31} & 0 & 0 & 0 \\ c_{23} & c_{22} & c_{21} & 0 & 0 & 0 \\ c_{13} & c_{12} & c_{11} & 0 & 0 & 0 \\ 0 & 0 & 0 & c_{44} & 0 & 0 \\ 0 & 0 & 0 & 0 & c_{66} & 0 \\ 0 & 0 & 0 & 0 & 0 & c_{55} \end{bmatrix}$$

$$e_{ANSYS} = \begin{bmatrix} e_{33} & 0 & 0 \\ e_{23} & 0 & 0 \\ e_{13} & 0 & 0 \\ 0 & 0 & 0 \\ 0 & 0 & 0 \\ 0 & 0 & 0 \end{bmatrix}, \quad \varepsilon_{ANSYS} = \begin{bmatrix} \varepsilon_{33} & & \\ & \varepsilon_{22} & \\ & & \varepsilon_{11} \end{bmatrix}$$

(1)

Electrodes across the surfaces of PVDF films are modeled as coupled elements. From the experimental observation, as the driving frequency is over 1254 Hz, both the output voltage and power become much smaller. Hence in the modal analysis, the range of the simulation conducted is set within 0 – 1200 Hz. Calculated resonant frequencies of the first 7 modes of a single cylindrical shell device are 156.336 Hz, 173.121 Hz, 362.856 Hz, 403.665 Hz, 896.086 Hz, 913.901 Hz and 1160 Hz. The corresponding mode shapes of the piezoelectric layer are shown as Figure 2, in which the first mode is the torsional mode, and second and sixth modes are pure bending modes in vertical direction. As for the third and fourth modes,

5

bending and torsional modes exist simultaneously, while the torsional motion dominates in the third mode

and the bending motion dominates in the fourth mode. In Figure 2(e), both the vertical and lateral bending

modes can be observed in the fifth mode. For the seventh mode, only extension motion along the length

direction can be obtained. As for the double wall cylindrical structure, there are ten modes that can be

obtained and the resonant frequencies are calculated to be 57.475 Hz, 63.768 Hz, 253.726 Hz, 343.428 Hz,

419.335Hz, 422.48Hz, 823.441 Hz, 861.79 Hz, 1032 Hz and 1200 Hz respectively. Double-wall structure has

more modes number than the single wall structure, since the response spectral density of the displacement of

the piezoelectric patch on the inner wall is increased by the coupling effect from the outer wall according to

the equation (35) in the reference [28].   As the extra resonant modes of the double wall structure are caused

through the coupling between the inner and the outer cylindrical shells, the frequencies of the extra modes

depending on the resonant modes of the outer shell, which are lower than those of the pure single wall

structure since the outer cylindrical shell with a large proof mass attached has lower resonant frequencies.

Similar to the results shown in Figure 2, pure vertical bending modes could be observed in Figures 3(b), 3(e)

and 3(g). The torsional motions exist in first, fourth and sixth modes. For the third mode, there exists both

vertical bending and longitudinal extension motions. Additionally, torsional and vertical bending motions

both appear in the eighth mode. As for the ninth and tenth modes, the lateral bending and torsional motions

are obtained. Harmonic analyses of both devices are also conducted for an intuitive comparison. In the

simulation, the displacement of the harmonic external excitation set to 0.6 μm is because with this external

excitation the output voltage at the resonant modes in the harmonic analysis is comparable with experimental

results. Also the displacement value of the external excitation in micrometer scale can be found in reference

[31] where the external excitation is set at 3.96 μm in the finite element analysis. The external load resistor is

set to be $10^{20}\Omega$ for open circuit. The driving frequency is swept from 0.5Hz to 1300 Hz with a step of

0.5Hz. Figures 4(a), 4(b) and 4(c) show the displacement in *x, y* and *z* directions of points along path 1

6

highlighted by a red line on the surface of the piezoelectric layer. From Figure 4 (a), it is obtained that the

inner cylinder of the double wall devices vibrates at around 57.5 Hz, 64 Hz, 254 Hz, 343 Hz, 419.5Hz, 823.5

Hz, 862 Hz, 1031.5 Hz and 1200 Hz through the harmonic analysis, which coincides with results of modal

analysis. In Figure 4(b), bending flexures along the path are observed at 63.5Hz, 253Hz, 419.5Hz, 823Hz

and 1031.5Hz. Especially at 63.5 Hz, 419.5 Hz, 823Hz and 1031.5Hz, the corresponding maximum values of

y displacements are 0.52μm, 1.12μm, 8μm and 0.60μm, compared with displacements in x and z directions,

whose values are calculated to be 0.17μm, 0.11μm, 1.33μm, 0.37μm, and 0.12μm, 0.04μm, 0.92μm, 0.24μm

respectively. With regard to the motions at 254 Hz, although the device vibrates both in the y and z directions

with maximum values of 0.51μm and 0.22μm, the displacement in the x direction is much larger 1.04μm.

For the frequencies of 57.5 Hz, 343Hz and 862 Hz, the displacements in x, y, and z directions are (0.025μm,

0.094μm, 0.11μm), (0.07μm, 0.13μm, 0.087μm), and (0.54μm, 3.01μm, 1.35μm) respectively. From these

results, it is found that the x axis displacement is relative small, which indicates that there is very small

extension along length direction. Meanwhile, for 57.5 Hz and 343Hz, since the y and z axis displacements

are comparable with each other, thickness shear mode across the y-z cross-section is induced. However, as

the y displacement at 862 Hz is relatively large, it is primarily bending rather than the thickness shear strain.

At 1200Hz, although values for the y and z displacements (0.3μm and 0.38μm respectively) are found to be

comparable, the x displacement (0.9μm) is almost three times of them. Finally, it should be noted that the

resonant frequency at 422.5 Hz is missing. This is because the mode at 422.5 Hz is too close to the mode at

419.5 Hz. In order to obtain a better idea of the mechanical energy in material and its potential for

piezoelectric energy harvesting, the displacement response has been normalized with respect to the base

acceleration corresponding to all resonant modes as shown in table 1. From the table, it is observed that the

maximum displacement responses among the first six modes are larger than the other modes, indicating that

the converting efficiencies at the first six modes are higher.

7

Table 1 Displacement response normalized with respect to the excitation acceleration for the double wall

cylindrical device

	x- direction (µm/g)	y- direction (µm/g)	z- direction (µm/g)
1st mode at 57.5 Hz	0.32	1.20	1.41
2nd mode at 64 Hz	1.75	5.37	1.24
3rd mode at 254 Hz	0.68	0.33	0.14
4th mode at 343 Hz	0.03	0.05	0.03
5th mode at 419.5 Hz	0.03	0.27	0.01
6th mode at 823.5 Hz	0.08	0.50	0.06
7th mode at 862 Hz	0.03	0.17	0.08
8th mode at 1031.5 Hz	0.01	0.02	0.01
9th mode at 1200 Hz	0.03	0.01	0.01

Peak-to-peak output voltages across the piezoelectric layers in both configurations are also obtained. It is

found that the first and second peaks of the output voltage of the double-wall cylindrical device at 64Hz and

253.5 Hz are 0.7 mV and 3.1 mV respectively. With the driving frequency increases to 420Hz, the output

voltage is 73.7 mV. The output voltage is 337.5 mV at the transverse vibration frequency of 823.5 Hz. The

output voltages, 41.3 mV and 62.9mV, of the fifth (1041.5Hz) and sixth mode (1208.5 Hz) are obtained

respectively. Correspondingly, output voltages of 9.2 mV, 5.9mV, 14.6 mV, 278.9 mV and 56 mV of the

single cylindrical device are obtained when the driven frequencies are at 173 Hz, 363 Hz, 404.5 Hz, 914.5

Hz and 1168Hz respectively. From the obtained results, we can relate the output voltages as shown in Figure

8

5 to the longitudinal and transverse bending motions. Comparing the performances of these two configurations, it is found that the output voltage at 823.5 Hz of the double wall cylindrical device is 1.21 times higher than that of the single wall device at 914.5 Hz. Similar as the displacement response, the output voltage of both devices are normalized with respect to the input acceleration. The results are shown as Table 2. There are five modes that can be utilized for the single wall device, whose output voltage response are ranged from 1.89 mV/g to 14.09 mV/g. From results of double wall devices, there are six modes ranging from 1.61 mV/g to 21.03 mV/g. Overall the double-wall device has more induced resonant modes and wider output ranges at the same external excitation level .

Table 2 Output voltage responses normalized with respect to the base acceleration for both single and double

wall cylindrical devices

	1st mode	2nd mode	3rd mode	4th mode	5th mode	6th mode
Single wall	12.99 mV/g @ 173 Hz	1.89 mV/g @ 363 Hz	3.77 mV/g @ 404.5 Hz	14.09 mV/g @ 914.5 Hz	2.83 mV/g @ 1168 Hz	
Double wall	7.23 mV/g @ 64 Hz	2.04 mV/g @ 253.5 Hz	17.66 mV/g @ 420 Hz	21.03 mV/g @ 823.5 Hz	1.61 mV/g @ 1041.5 Hz	1.82 mV/g @ 1208.5 Hz

4 Experiments

Figure 6 shows the experimental setup including: (1) TTi TG 1010A function generator, (2) mechanical shaker (LDS V406), (3) Tektronix TDS 1001B oscilloscope and (4) Agilent 34405A digital multimeter (DMM). Figure 6(b) is the zoomed out figure for the double wall cylindrical energy harvesting device. The output voltage was taken from the oscilloscope. When conducting the harmonic measurement of the device, the driven frequency is swept from 15Hz to 1275Hz, and the driving voltage for the shaker is set at 12V. All

9

the external load resistances are characterized using the Agilent 34405A digital multimeter.

4.1 Measurements of the single wall harvester

In order to demonstrate the advantages of the double-wall piezoelectric cylindrical energy harvester, the single wall device was firstly characterized for comparison. The first step was to conduct a frequency sweeping analysis with an open electric circuit. In order to avoid lengthy measurement, the swept step is set to be 1 Hz near the resonant frequencies and 5Hz far away from the resonant points. Figure 7(a) and 7(b) show the output peak-peak voltage and root mean square root voltage versus the excitation frequency. From the results, it is observed that the fundamental resonant frequency is 154.6 Hz where peak-peak and RMS values are 276 mV and 81.2 mV. The ratio between these two values is 3.4, which is a little different from the theoretical ratio 2.828($V_{peak-peak} = 2\sqrt{2}V_{rms}$). The difference can be explained as the output voltage is not an ideal sinusoidal wave. The varying trend of output voltage versus frequency relationship is obvious in the figure. In addition, there are several small fluctuations around 112 Hz, 424Hz, 738Hz, 926Hz in circled areas. That is probably due to that bending modes are not being fully excited. The optimum load resistance can be determined at the resonant frequency 156.3 Hz. In order to conduct a systematic analysis on the relationship between the output performance and the load resistance, the selected resistances are varied from 9.79 kΩ to 53.7 MΩ. From Figures 8(a) and 8(b), it is observed that the output voltage rapidly increases with the load resistance from 9.79 kΩ to 5.56 MΩ. After that, the output voltage will keep steady at 0.36 V and 0.115 V respectively. From the output voltage U and the load resistance R, the output power P is calculated as

$$P = \frac{U^2}{R} \qquad (2)$$

Figures 8(c) and 8(d) illustrates the output power versus the load resistance in the logarithmic scale. The curves are Gaussian shaped, where the maximum peak-to-peak and RMS values are 44.4 nW and 3.94 nW.

10

The corresponding optimum resistance is 1.05 MΩ.

4.2 Characterization of double-wall harvester

Compared with the single wall piezoelectric energy harvester, the double wall harvester shows more resonant modes. Frequencies for these resonant modes are 48Hz, 92Hz, 620Hz, 860Hz, 948Hz, 1079Hz, 1135Hz and 1254Hz respectively. The peak-peak output voltages corresponding to these frequencies are 0.286 V, 0.113 V, 0.34V, 0.416 V, 0.214 V, 0.136 V, 0.372 V and 0.264 V. RMS voltages are 0.0548 V, 0.0265 V, 0.103 V, 0.13 V, 0.0597 V, 0.0336 V, 0.115 V and 0.0768 V. When the driving frequency is tuned over 1300 Hz, no higher modes can be observed. Combined with Figures 5, 7 and 9, it is concluded that although the experimental results of resonant frequencies do not exactly match with the numerical analysis, the similar trends of voltage responses are still justified both for single wall and double wall devices. From the data shown in Figures 9(a) and 9(b), the *Q* factor is calculated through

$$Q = \frac{f_{r_i}}{\Delta f_i} \qquad (3)$$

Where f_{r_i} and Δf_i represent resonant frequency and half power bandwidth respectively for mode *i*. Q factors corresponding to the eight modes are calculated to be 43.78, 19.1, 97.49, 85.85, 48.6, 72.16, 390.36, and 403.49. Low quality factor values indicate the device has wider response frequency band, which is advantageous for harvesting more environmental vibrations. Table 5 summarizes the quality factors for the double wall device. The relationship between the output voltage and the load resistance for the double wall device has been characterized as shown in Figures 10(a) and 10(b). With increasing external load resistance, the output voltage increases abruptly at the beginning. When the resistance reaches up to 2.642 MΩ, the voltage gets saturated. It is seen that the output voltages at 614 Hz, 866 Hz, 1136 Hz are about two times

11

higher than other modes. This may be attributed to the bending motions of the piezoelectric layer dominating in these modes. The output power versus the load resistance is shown in Figures 10(c) and 10(d). The optimum load resistances, 1.136 MΩ, 1.05 MΩ, 491.7 KΩ, 427 KΩ, 310.96 KΩ, 310.96 KΩ, 310.96 KΩ and 310.96 KΩ, corresponding to these eight modes have been obtained. As the external load resistance corresponding to the maximum output power is calculated by $1/(\omega C)$, and the capacitance C is the generated charge divided by the output voltage $V/(\omega Q)$. ωQ is equal to the amplitude of the AC current. Therefore when the resonant frequency increases, the optimal load resistance decreases.   The maximal output power appears at 1136 Hz where the value for peak-peak power is 134 nW. The maximum peak-peak output powers for 48 Hz, 91 Hz, 614 Hz, 866 Hz, 926 Hz, 1056 Hz and 1254 Hz are 13.54 nWatt, 6.72 nW, 107.59 nW, 81.02 nW, 23.56 nW, 14.7 nW and 54.35 nW, and maximum RMS output powers are 0.499 nW, 0.358 nW, 9.97 nW, 7.45 nW, 5.89 nW, 4.79 nW and 4.64 nW respectively. The result of optimum resistance versus the resonant frequency is shown in Figure 11.

In order for a clear comparison, the output voltages of the two devices are normalized with respect to the base acceleration (characterizing the efficiency), and the results are shown in tables 3. It is found that with the increased external driving frequency, the normalized output voltage is undermined. The first five modes having relatively large output are usable. While for the double wall device, there are eight modes that are usable. Table 4 shows the results of output powers normalized with respect to the base acceleration for both single and double wall cylindrical devices. For the single wall device, only the mode at 156.3 Hz can be examined where the output power with respect to the base acceleration is 4.61×10^{-5} (nW·m)/g. As for the double wall device, the result is ranging from 3.34×10^{-7} to 1.49×10^{-4} (nW·m)/g. With the driving frequency increases, the output power decreases gradually from mode 1 to mode 6.

12

Table 3 Output voltage responses normalized with respect to the base acceleration for both single and double

wall cylindrical devices

	1st mode	2nd mode	3rd mode	4th mode	5th mode	6th mode	7th mode	8th mode
Single wall	1.54×10^{-7} (V·m)/g @ 112 Hz	2.93×10^{-7} (V·m)/g @ 154.6 Hz	1.05×10^{-8} (V·m)/g @ 424 Hz	5.26×10^{-9} (V·m)/g @ 738Hz	3.61×10^{-9} (V·m)/g @ 926 Hz			
Double wall	3.15×10^{-6} (V·m)/g @ 48 Hz	3.39×10^{-7} (V·m)/g @ 92 Hz	2.24×10^{-8} (V·m)/g @ 620 Hz	1.43×10^{-8} (V·m)/g @ 860Hz	6.04×10^{-9} (V·m)/g @ 948 Hz	2.96×10^{-9} (V·m)/g @ 1079 Hz	7.32×10^{-9} (V·m)/g @1135 Hz	4.26×10^{-9} (V·m)/g @1254 Hz

Table 4 Output power responses normalized with respect to the base acceleration for both single and double

wall cylindrical devices

	1st mode	2nd mode	3rd mode	4th mode	5th mode	6th mode	7th mode	8th mode
Single wall		4.61×10^{-5} (nW·m)/g @ 156.3 Hz						
Double wall	1.49×10^{-4} (nW·m)/g @ 48 Hz	2.06×10^{-5} (nW ·m)/g @ 91 Hz	7.24×10^{-6} (nW ·m)/g @ 614 Hz	2.74×10^{-6} (nW ·m)/g @ 866Hz	6.97×10^{-7} (nW ·m)/g @ 926 Hz	3.34×10^{-7} (nW ·m)/g @ 1056 Hz	2.63×10^{-6} (nW ·m)/g @1136 Hz	8.76×10^{-7} (nW ·m)/g @1254 Hz

The multimode response of presented device is attributed to the circular cross-section and the large

aspect ratio of cylinders, which makes it easy to be excited in both circumferential and longitudinal

13

directions. Especially for longer cylinder, more longitudinal and bending modes can be seen [25]. It should

be noted that the L-shaped connection could introduce some energy loss through its oscillations, which can

be overcome by further optimized mechanical designs. Vibrations of the inner cylinder can be coupled into

the outer cylinder and vise versa through the mass attached to the end of the inner cylinder by knocking

effect. This knocking is a potential advantage as more resonating modes can be generated. Although the

harvested power is only at level of 100 nW, it is enough to power the 32 kHz quartz oscillator [32].

Furthermore, it is possible to miniaturize it into much smaller scales using micromachining processes.

4.3 Dynamic response of double-wall cylindrical energy harvesting device

It is necessary to characterize the output performance of the device under different driven voltages.

Figures 12(a)-12(h) demonstrate the relation between peak-peak output voltage and the driving frequency for

different excitation amplitudes, 5 V, 10 V and 16 V. The frequency band width in the measurement at each

mode is set to be 41 Hz. External resistances for the eight resonant modes are all set to be optimum

resistances, which are 601 KΩ, 601 KΩ, 491.7 KΩ, 491.7 KΩ, 427 KΩ, 427 KΩ, 310.96 KΩ and 310.96 KΩ

respectively. The experiment has been repeated dozens of times, which caused shifting of the optimum load

resistance at the first two modes. While the load resistances for the other modes still match with previous

characterizations. Measurements show that the output voltages at the first mode, second mode, fifth mode,

sixth mode and eighth mode are lower than the voltages at third, fourth and seventh mode. Furthermore, the

output voltage increases with the increasing external driving voltage. Figure 12(a) shows the peak-peak

output voltages corresponding to driving voltages of 5 V, 10 V and 16 V are 63.2 mV, 88 mV and 110 mV

respectively, and the corresponding resonant frequencies are 49 Hz, 49 Hz and 48 Hz. It should be noted that

there is one Hertz shift when the driven voltage is set at 16 V. The oscilloscope used in the experiment is the

14

40 MHz bandwidth TDS 1001B and the time base range is from 5 ns to 50 s/div, so the smallest frequency it

can measure is 0.02 Hz. The similar pattern can be found in Figure 12(b). In Figure 12(c), the maximum

peak-peak voltages are 124 mV at 622 Hz for 5 V driving, 170 mV at 621 Hz for 10 V driving , and 232 mV

at 619 Hz for 15 V driving. In Figure 12(d), the resonant frequencies for 5 V and 15 V driving are the same at

859 Hz, where the output voltages are 166 mV and 272 mV respectively. When the device is driven at 10 V,

the output voltage is 250 mV at 857 Hz. The quality factors are quite different with each other, which are

106.52, 128.10 and 54.5. In the fifth resonant mode (Figure 12(e)), the resonant frequency shifts down when

the external voltage increases from 5 V to 15 V. The corresponding resonant frequencies are 957 Hz, 953 Hz

and 948 Hz. The peak-peak output voltages are shown to be 80.8 mV, 110 mV and 136 mV respectively. And

the quality factors are 45.55, 52.05 and 43.84. In the sixth mode (Figure 12(f)), the corresponding measured

resonant frequencies are 1079 Hz, 1078 Hz and 1076 Hz, and the output peak-peak voltages are 62.4 mV,

84.8 mV and 110 mV. The quality factors are calculated as 34.28, 56.65 and 75.07. For the seventh mode

(Figure 12(g)), the resonant frequencies for the three external excitations are the same as 1131 Hz. The

maximum peak-peak voltages are 120 mV, 188 mV and 244 mV. The quality factors are 374.5, 316.81 and

363.67. In Figure 12(h), the resonant frequencies for 10 V and 15 V driving have two Hertz shift from the

resonant frequency at 5 V driving. The peak-peak voltage for 5 V driving is 78.4 mV at 1254 Hz. The

peak-peak voltage for 10 V and 15 V driving are 125 mV and 162 mV respectively. The quality factors are

257.26, 359.77 and 166.12. From these results, it is found that as the external excitation increases, the output

voltage will be improved. However, at higher driving voltages the quality factors will usually be undermined

and more energy will be dissipated in the mechanical vibrations. The quality factors corresponding to all

modes at these three driving voltages are listed in Table 5. Table 6 summarizes the normalized output power,

from which it displays the same trend as in Table 4. Furthermore, it provides information about the

normalized output power varying with the driving voltage from 5 V to 15 V. It means that when the

15

excitation increases, the energy converting efficiency is improved correspondingly. Table 7 compares the performance of our model with previous reported prototypes in the viewpoint of energy harvesting from multimode mechanical response. Although the normalized output power density range does not show any superiority than other types of devices, this work does exhibit a widened response from multimode vibrations.

Table 5 Quality factors of double wall cylindrical devices

	1st mode	2nd mode	3rd mode	4th mode	5th mode	6th mode	7th mode	8th mode
Driven @ 5 Volt	<1.2 @ 49 Hz	<2.24 @ 92 Hz	117.17 @ 622 Hz	104.92 @ 859 Hz	45.55 @ 957 Hz	34.28 @ 1079 Hz	374.5 @1131 Hz	257.26 @1254 Hz
Driven @ 10 Volt	19.3 @ 49 Hz	<2.22 @ 91 Hz	80.95 @ 621 Hz	74.06 @ 857 Hz	52.05 @ 953 Hz	56.65 @ 1078 Hz	316.81 @1131 Hz	359.77 @1252 Hz
Driven @ 15 Volt	19.14 @ 48 Hz	13 @ 91 Hz	83.88 @ 619 Hz	54.40 @ 859 Hz	43.84 @ 948 Hz	75.07 @ 1076 Hz	363.67 @1131 Hz	166.12 @1252 Hz

Table 6 The power normalized with respect to driven frequency for double wall cylindrical device, (nW·m)/g

	1st mode	2nd mode	3rd mode	4th mode	5th mode	6th mode	7th mode	8th mode
Driven @ 5 Volt	2.768×10^{-3}	6.89×10^{-4}	8.083×10^{-5}	7.595×10^{-5}	1.669×10^{-5}	7.8325×10^{-6}	3.6202×10^{-5}	1.257×10^{-5}
Driven @ 10 Volt	5.53666×10^{-3}	9.0736×10^{-4}	1.5241×10^{-4}	1.7307×10^{-4}	3.1201×10^{-5}	1.4492×10^{-5}	8.8856×10^{-5}	3.2056×10^{-5}
Driven @ 15 Volt	8.738×10^{-3}	1.391×10^{-3}	2.857×10^{-4}	2.039×10^{-4}	4.82×10^{-5}	2.448×10^{-5}	1.497×10^{-4}	5.384×10^{-5}

16

Table 7 Performance comparison between proposed device and previous references

Reference	Volume of piezoelectric layer (mm³)	Resonant frequencies (Hz)	Normalized output power density range (nW·m)/(mm³·g)
Reference [33]	125×105×1.02	804.05/1499.75	$1.39×10^{-7}$—$4.76×10^{-6}$
Reference [34]	8.5×10×0.127 —stage 1 8.5×5×0.127—stage 2 8.5×2.5×0.127—stage 3	34.5/73.7/124.9	$6.48×10^{-3}$— 0.1811
Reference [35]	440	40/140	$6.09×10^{-2}$—1.32
Reference [36]	$1.675×10^{-2}$	380	0—$2.05×10^{-2}$
Prototype in this work	50×5×0.11	48/91/614/866/926/1056/1136/1254	$3.19×10^{-8}$—$5.42×10^{-6}$

4   Conclusion

A double-wall piezoelectric cylindrical resonator for harvesting multi-modal mechanical vibrations has been presented in this paper. From the numerical analysis, it shows that ten vibration modes have been demonstrated. In experiment eight vibration modes are observed and can be utilized for energy harvesting, and the rest two modes have no power output possibly due to charge cancellation in torsional deformations. Both voltage and power responses corresponding to each resonant mode have been characterized. Through the measurement, the outputs for resonant modes of 614 Hz, 866 Hz and 1135 Hz are comparably higher, and the outputs at 48 Hz, 91 Hz, 926 Hz, 1056 Hz and 1254 Hz are slightly lower, which could be attributed to the mode shape difference. Prototypes of a single and a double wall cylindrical harvester have been characterized and compared. By measuring the resonance frequencies, the Q factor, the output voltage, the optimum load resistance and calculating the power generated under different driving voltages, it is shown that the double wall cylindrical energy harvester has more resonant modes and higher energy converting

17

efficiency. The dynamic response of each resonating mode corresponding to different external excitations has also been presented. By comparing the performance of our device with previous reported prototypes in the viewpoint of energy harvesting from multimode mechanical response, the widest working frequency range (48Hz – 1254 Hz) and the most number of workable oscillation modes have been demonstrated.

References:

1. Kausar, A.S.M.Z., et al., *Energizing wireless sensor networks by energy harvesting systems: Scopes, challenges and approaches.* Renewable & Sustainable Energy Reviews, 2014. **38**: p. 973-989.

2. Annamdas, V.G.M. and M.A. Radhika, *Electromechanical impedance of piezoelectric transducers for monitoring metallic and non-metallic structures: A review of wired, wireless and energy-harvesting methods.* Journal of Intelligent Material Systems and Structures, 2013. **24**(9): p. 1021-1042.

3. Aktakka, E.E., H. Kim, and K. Najafi, *Energy scavenging from insect flight.* Journal of Micromechanics and Microengineering, 2011. **21**(9).

4. Banal, J.L., K.P. Ghiggino, and W.W.H. Wong, *Efficient light harvesting of a luminescent solar concentrator using excitation energy transfer from an aggregation-induced emitter.* Physical chemistry chemical physics : PCCP, 2014. **16**(46): p. 25358-63.

5. Hudak, N.S. and G.G. Amatucci, *Small-scale energy harvesting through thermoelectric, vibration, and radiofrequency power conversion.* Journal of Applied Physics, 2008. **103**(10).

6. Zhu, D., et al., *Increasing output power of electromagnetic vibration energy harvesters using improved Halbach arrays.* Sensors and Actuators a-Physical, 2013. **203**: p. 11-19.

7. Mitcheson, P.D. and T.C. Green, *Maximum Effectiveness of Electrostatic Energy Harvesters When Coupled to Interface Circuits.* Ieee Transactions on Circuits and Systems I-Regular Papers, 2012. **59**(12): p. 3098-3111.

8. Karami, M.A. and D.J. Inman, *Parametric Study of Zigzag Microstructure for Vibrational Energy Harvesting.* Journal of Microelectromechanical Systems, 2012. **21**(1): p. 145-160.

9. Pan, C.T., et al., *Design and fabrication of flexible piezo-microgenerator by depositing ZnO thin films on PET substrates.* Sensors and Actuators a-Physical, 2010. **159**(1): p. 96-104.

10. Roundy, S., et al., *Improving power output for vibration-based energy scavengers.* Ieee Pervasive Computing, 2005. **4**(1): p. 28-36.

11. Liu, J.-Q., et al., *A MEMS-based piezoelectric power generator array for vibration energy harvesting.* Microelectronics Journal, 2008. **39**(5): p. 802-806.

12. Schaufuss, J., D. Scheibner, and J. Mehner, *New approach of frequency tuning for kinetic energy harvesters.* Sensors and Actuators a-Physical, 2011. **171**(2): p. 352-360.

13. Liu, H., et al., *Enhancing output power of a piezoelectric cantilever energy harvester using an oscillator.* Smart Materials and Structures, 2012. **21**(6).

14. Zhou, W., G.R. Penamalli, and L. Zuo, *An efficient vibration energy harvester with a multi-mode dynamic magnifier.* Smart Materials and Structures, 2012. **21**(1).

15. Lee, S. and B.D. Youn, *A New Piezoelectric Energy Harvesting Design Concept: Multimodal Energy Harvesting Skin.* Ieee Transactions on Ultrasonics Ferroelectrics and Frequency Control, 2011. **58**(3): p. 629-645.

16. Lee, S. and B.D. Youn, *A design and experimental verification methodology for an energy harvester skin structure.* Smart Materials and Structures, 2011. **20**(5).

17. Bai, X., et al., *Multi-modal vibration energy harvesting utilizing spiral cantilever with magnetic coupling.*

18

Sensors and Actuators a-Physical, 2014. **209**: p. 78-86.

18. Chew, Z. and L. Li, *Design and characterisation of a piezoelectric scavenging device with multiple resonant frequencies.* Sensors and Actuators A: Physical, 2010. **162**(1): p. 82-92.

19. Yang, J.S. and R.C. Batra, *THICKNESS-SHEAR VIBRATIONS OF A CIRCULAR CYLINDRICAL PIEZOELECTRIC SHELL.* Journal of the Acoustical Society of America, 1995. **97**(1): p. 309-312.

20. Wu, G., et al., *Resonance magnetoelectric effect in radially polarized long cylindrical composite structures.* Journal of Applied Physics, 2013. **113**(21).

21. Hagood, N.W. and A.J. McFarland, *MODELING OF A PIEZOELECTRIC ROTARY ULTRASONIC MOTOR.* Ieee Transactions on Ultrasonics Ferroelectrics and Frequency Control, 1995. **42**(2): p. 210-224.

22. Kagawa, Y., et al., *Finite element simulation of dynamic responses of piezoelectric actuators.* Journal of Sound and Vibration, 1996. **191**(4): p. 519-538.

23. Kielczynski, P. and M. Szalewski, *Compound piezoelectric cylindrical resonators as sensors of the rheological parameters of viscoelastic media.* Ieee Transactions on Ultrasonics Ferroelectrics and Frequency Control, 2007. **54**(6): p. 1199-1206.

24. Wakatsuki, N., Y. Kagawa, and M. Haba, *Tri-axial sensors and actuators made of a single piezoelectric cylindrical shell.* Ieee Sensors Journal, 2004. **4**(1): p. 102-107.

25. Mazeika, D., et al., *New cylindrical piezoelectric actuator based on traveling wave.* Mechanical Systems and Signal Processing, 2013. **36**(1): p. 127-135.

26. Xin, L., C. Kuochih, and T. Hornsen. *Energy harvesting using a circular cylindrical shell laminated with a segmented piezoelectric layer*. in *Piezoelectricity, Acoustic Waves and Device Applications (SPAWDA), 2010 Symposium on*. 2010.

27. Xu-fang, Z., H. Shun-di, and T. Horn-sen. *Experimental study of a piezoelectric ring energy harvester*. in *Piezoelectricity, Acoustic Waves and Device Applications (SPAWDA), 2013 Symposium on*. 2013.

28. Wang, C.Y. and R. Vaicaitis, *ACTIVE CONTROL OF VIBRATIONS AND NOISE OF DOUBLE WALL CYLINDRICAL SHELLS.* Journal of Sound and Vibration, 1998. **216**(5): p. 865-888.

29. Dowell, E.H., *Interior Noise Studies for Single- and Double-Walled Cylindrical Shells.* Journal of Aircraft, 1980. **17**(9): p. 690-699.

30. Dogan, V. and R. Vaicaitis, *Nonlinear Response of Double-Wall Cylindrical Shell Vibrations under Random Excitation.* Journal of Aerospace Engineering, 2006. **19**(1): p. 46-54.

31. Zhu, M., E. Worthington, and A. Tiwari, *Design study of piezoelectric energy-harvesting devices for generation of higher electrical power using a coupled piezoelectric-circuit finite element method.* Ultrasonics, Ferroelectrics, and Frequency Control, IEEE Transactions on, 2010. **57**(2): p. 427-437.

32. Vermesan, O. and P. Friess, eds. *Internet of Things: Converging Technologies for Smart Environments and Integrated Ecosystems*. 2013, River Publishers: Denmark.

33. Soobum, L. and B.D. Youn, *A new piezoelectric energy harvesting design concept: multimodal energy harvesting skin.* Ultrasonics, Ferroelectrics, and Frequency Control, IEEE Transactions on, 2011. **58**(3): p. 629-645.

34. Hu, Y. and Y. Xu, *A wideband vibration energy harvester based on a folded asymmetric gapped cantilever.* Applied Physics Letters, 2014. **104**(5): p. 053902.

35. Shindo, Y. and F. Narita, *Dynamic bending/torsion and output power of S-shaped piezoelectric energy harvesters.* International Journal of Mechanics and Materials in Design, 2014. **10**(3): p. 305-311.

36. Iannacci, J., et al., *Multi-modal vibration based MEMS energy harvesters for ultra-low power wireless functional nodes.* Microsystem Technologies, 2014. **20**(4-5): p. 627-640.

19

List of Figure Captions:

Figure 1. (a) Schematic diagram of the double-wall cylindrical energy harvesting device, which includes 1, L-shape fixture; 2, connecting plates used to connect outer cylinder with the fixture; 3, ribbed plates to enhance the stiffness of L-shape fixture; 4, screws to co-axially match the outer hollow cylinder with inner cylinder; 5, piezoelectric cylindrical patch; 6, outer hollow cylinder; 7, proof mass of outer cylinder; 8, inner hollow cylinder; 9, proof mass of inner cylinder; 10, screw holes to connect the assembled platform with vibrating shaker. (b) Cross-section at position A –A shown in figure 1(a), where $R_i, R_o, \alpha, t_i, t_p$ and t_o denote inner wall radius, outer wall radius, curved angle of piezoelectric layer, inner wall thickness, piezoelectric layer thickness and outer wall thickness, (c) inner cylindrical shell and (d) outer cylindrical shell.

Figure 2. Mode shapes of the piezoelectric layer of the single wall cylindrical device.

Figure 3. Mode shapes of the piezoelectric layer of double wall cylindrical device.

Figure 4. The displacement of the side edge of the piezoelectric patch (highlighted in red lines) on the double wall cylindrical device. (a), x displacement versus frequency; (b), y displacement versus frequency; (c), z displacement versus frequency.

Figure 5. Open circuit output voltages of single cylindrical and double cylindrical devices versus driven frequencies.

Figure 6. Experimental setup for double-wall piezoelectric cylindrical energy harvesting device. (a) The whole measured system including (1) TTi TG 1010A function generator, (2) mechanical shaker(LDS V406), (3) Tektronix TDS 1001B oscilloscope; (4) Agilent 34405A digital multimeter(DMM); (b) Zoomed out figure for the double wall cylindrical energy harvesting device.

Figure 7. Harmonic analysis of inner cylindrical energy harvesting device, (a)Peak-Peak voltage output; (b) RMS voltage.

Figure 8. (a) Peak-Peak voltage versus load resistance; (b) RMS voltage versus load resistance. (c) Output peak-peak power versus load resistance; (d) Output RMS power versus load resistance.
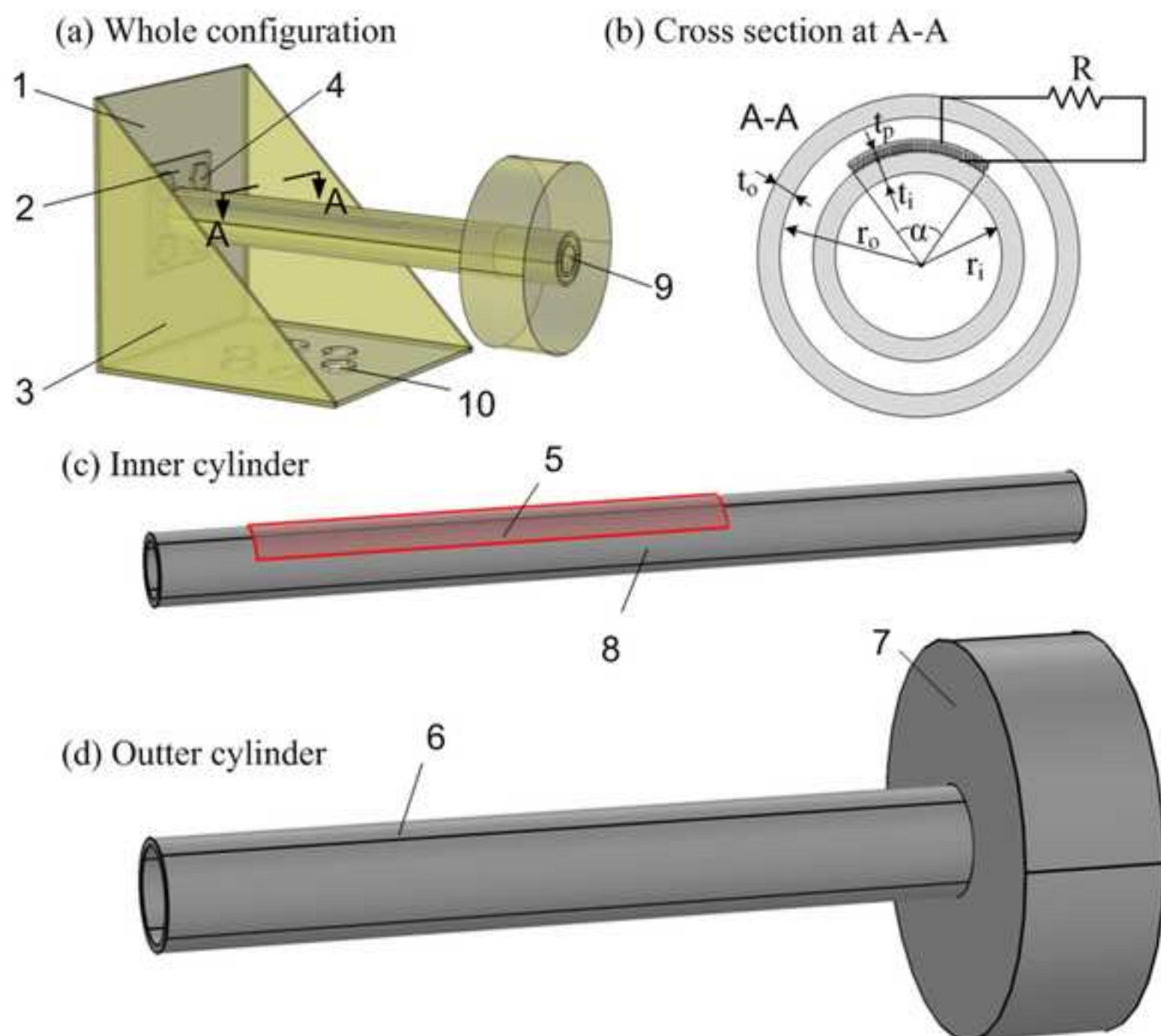
Figure 9. (a) Harmonic analysis of double-wall cylindrical energy harvesting device, Peak-Peak voltage output; (b) Harmonic analysis of double-wall cylindrical energy harvesting device, RMS voltage output.

Figure 10. (a) Peak-Peak voltage versus load resistance at different modal resonant frequencies; (b) RMS voltage versus load resistance at different modal resonant frequencies. (c) Output peak-peak power versus load resistance in logarithmic scale for multiwall cylindrical energy harvesting device; (d) Output RMS power versus load resistance in logarithmic scale for multiwall cylindrical energy harvesting device.
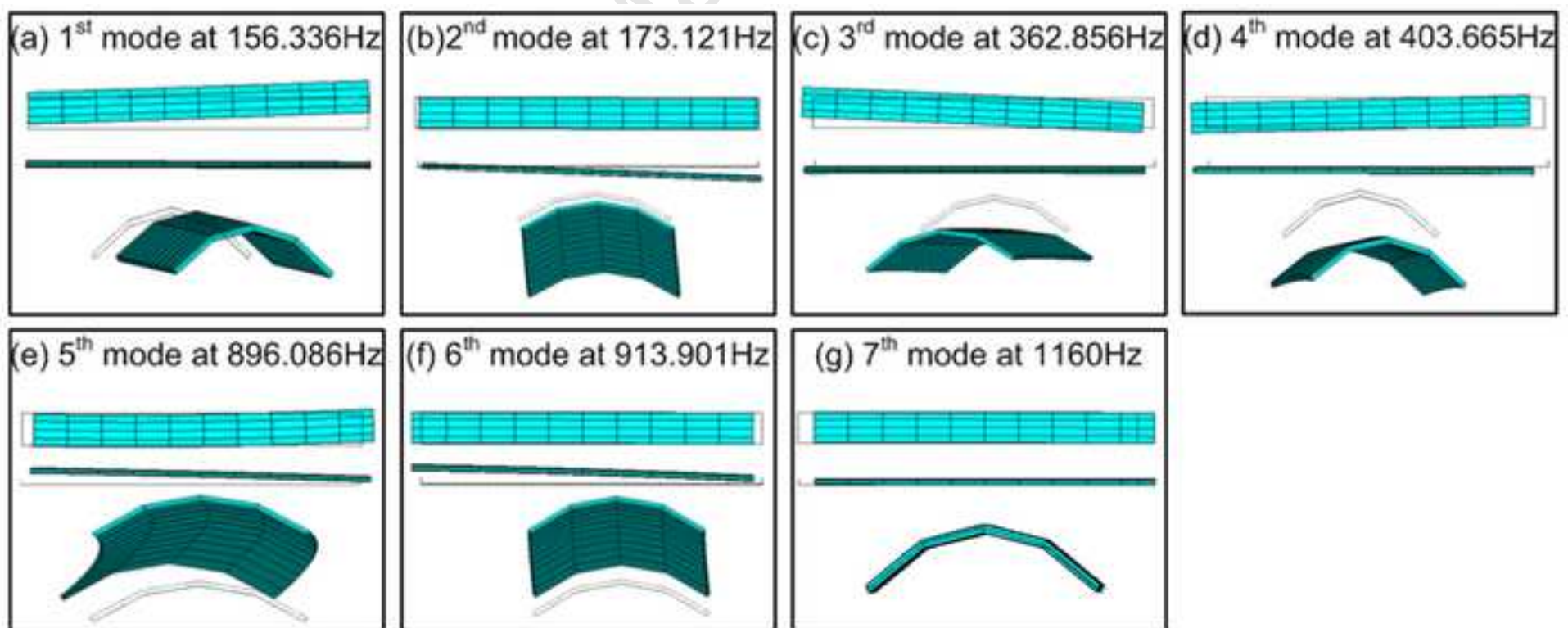
Figure 11. Optimum load resistance versus resonant frequency.

Figure 12. Output dynamic response corresponding to eight resonant modes at different external excitations.

20

(a) Whole configuration

1
2
3
4

A
A

9
10

(b) Cross section at A-A

R

A-A

t_p
t_o
t_i
r_o
α
r_i

(c) Inner cylinder

5
8

(d) Outter cylinder

6
7

(a) 1st mode at 156.336Hz
(b) 2nd mode at 173.121Hz
(c) 3rd mode at 362.856Hz
(d) 4th mode at 403.665Hz
(e) 5th mode at 896.086Hz
(f) 6th mode at 913.901Hz
(g) 7th mode at 1160Hz

(a) 1st mode at 57.475Hz
(b) 2nd mode at 63.768Hz
(c) 3rd mode at 253.726Hz
(d) 4th mode at 343.428Hz
(e) 5th mode at 419.335Hz
(f) 6th mode at 422.48Hz
(g) 7th mode at 823.441Hz
(h) 8th mode at 861.79Hz
(i) 9th mode at 1032Hz
(j) 10th mode at 1200Hz

(a)   (b)   (c)

(a)   (b)

(a)

(b)

Optimum load resistance versus resonant frequency

ACCEPTED MANUSCRIPT

List of Figure Captions:

Figure 1. (a) Schematic diagram of the double-wall cylindrical energy harvesting device, which includes 1, L-shape fixture; 2, connecting plates used to connect outer cylinder with the fixture; 3, ribbed plates to enhance the stiffness of L-shape fixture; 4, screws to co-axially match the outer hollow cylinder with inner cylinder; 5, piezoelectric cylindrical patch; 6, outer hollow cylinder; 7, proof mass of outer cylinder; 8, inner hollow cylinder; 9, proof mass of inner cylinder; 10, screw holes to connect the assembled platform with vibrating shaker. (b) Cross-section at position A –A shown in figure 1(a), where $R_i, R_o, \alpha, t_i, t_p$ and t_o denote inner wall radius, outer wall radius, curved angle of piezoelectric layer, inner wall thickness, piezoelectric layer thickness and outer wall thickness, (c) inner cylindrical shell and (d) outer cylindrical shell.

Figure 2. Mode shapes of the piezoelectric layer of the single wall cylindrical device.

Figure 3. Mode shapes of the piezoelectric layer of double wall cylindrical device.

Figure 4. The displacement of the side edge of the piezoelectric patch (highlighted in red lines) on the double wall cylindrical device. (a), x displacement versus frequency; (b), y displacement versus frequency; (c), z displacement versus frequency.

Figure 5. Open circuit output voltages of single cylindrical and double cylindrical devices versus driven frequencies.

Figure 6. Experimental setup for double-wall piezoelectric cylindrical energy harvesting device. (a) The whole measured system including (1) TTi TG 1010A function generator, (2) mechanical shaker(LDS V406), (3) Tektronix TDS 1001B oscilloscope; (4) Agilent 34405A digital multimeter(DMM); (b) Zoomed out figure for the double wall cylindrical energy harvesting device.

Figure 7. Harmonic analysis of inner cylindrical energy harvesting device, (a)Peak-Peak voltage output; (b) RMS voltage.

Figure 8. (a) Peak-Peak voltage versus load resistance; (b) RMS voltage versus load resistance. (c) Output peak-peak power versus load resistance; (d) Output RMS power versus load resistance.

Figure 9. (a) Harmonic analysis of double-wall cylindrical energy harvesting device, Peak-Peak voltage output; (b) Harmonic analysis of double-wall cylindrical energy harvesting device, RMS voltage output.

Figure 10. (a) Peak-Peak voltage versus load resistance at different modal resonant frequencies; (b) RMS voltage versus load resistance at different modal resonant frequencies. (c) Output peak-peak power versus load resistance in logarithmic scale for multiwall cylindrical energy harvesting device; (d) Output RMS power versus load resistance in logarithmic scale for multiwall cylindrical energy harvesting device.

Figure 11. Optimum load resistance versus resonant frequency.

Figure 12. Output dynamic response corresponding to eight resonant modes at different external excitations.

Highlights for the manuscript: "Double-wall piezoelectric cylindrical energy harvester"

- A double wall cylindrical structure has been designed, simulated, fabricated, and characterized for energy harvesting.

- The device has advantages of multiple resonant frequencies, and capability of responding multi-directional environmental vibrations.

Mr. Jie Mei is PhD student at College of Engineering, Swansea University. His research interests are energy harvesting, micro&nano systems. He has published around 10 articles in this field.

Dr. Lijie Li is associate professor at College of Engineering, Swansea University. His research interests are mechanical, electrical and Microsystems. He has published over 100 articles in related fields.